Exp Fluids
DOI 10.1007/s00348-012-1357-6

RESEARCH ARTICLE

A vision-based hybrid particle tracking velocimetry (PTV) technique using a modified cascade correlation peak-finding method

Y.-C. Lei · W.-H. Tien · J. Duncan · M. Paul · N. Ponchaut · C. Mouton · D. Dabiri · T. Rösgen · J. Hove

Received: 1 August 2010 / Revised: 6 July 2012 / Accepted: 23 July 2012

Abstract A novel technique for particle tracking velocimetry is presented in this paper to overcome the issue of overlapping particle images encountered in the flows with high particle density or under volumetric illumination conditions. To achieve this goal, algorithms for particle identification and tracking are developed based on current methods and validated with both synthetic and experimental image sets. The results from synthetic image tests show that the particle identification algorithm is able to resolve overlapped particle images up to 50 % under noisy conditions, while keeping the root mean square peak location error under 0.07 pixels. The algorithm is also robust to the size changes up to a size ratio of 5. The tracking method developed from a classic computer vision matching algorithm is capable of capturing a velocity gradient up to 0.3 while maintaining the error under 0.2 pixels. Sensitivity tests were performed to describe the optimum conditions for the technique in terms of particle image density, particle image sizes and velocity gradients, also its sensitivity to errors of the PIV results that guide the tracking process. The comparison with other existing tracking techniques demonstrates that this technique is able to resolve more vectors out of a dense particle image field.

Y.-C. Lei · W.-H. Tien · J. Duncan · M. Paul · D. Dabiri (✉)
Department of Aeronautics and Astronautics,
University of Washington, Seattle, WA 98195, USA
e-mail: dabiri@aa.washington.edu

Y.-C. Lei
Performance Group Division, Canadian Aviation Electronics Inc., 8585 Chemin de la Côte de Liesse, Saint-Laurent, Quebec, CA H4T 1G6, Canada

J. Duncan
118 N Wolfe Ave Bldg 1643, Edwards Air Force Base, CA 93524, USA

M. Paul
205 W D Ave, Building 350, Eglin Air Force Base, FL 32542, USA

N. Ponchaut
Exponent, 9 Strathmore Rd., Natick, MA 01760, USA

C. Mouton
RAND Corporation, 1776 Mail St., Santa Monica, CA 90407, USA

T. Rösgen
Institute of Fluid Dynamics, ETH Zurich, 8092 Zurich, Switzerland

J. Hove
Molecular and Cellular Physiology, University of Cincinnati College of Medicine, 231 Albert Sabin Way, Cincinnati, OH 45267, USA

1 Introduction

Particle tracking velocimetry (PTV) has long been a valuable technique to investigate small-scale flow structures, dating back to the time of Da Vinci (Gharib et al. 2002). In the last several decades, computational advances have made it possible to automate PTV processes, initially by obtaining quantitative measurements based on streaking motions of tracer particles, as summarized by Agui and Jimenez (1987). Algorithmically, progress was made in the 1990s with the introduction of two-frame (rather than four-frame) particle tracking routines by researchers such as Baek and Lee (1996), whereby particles were matched based on their "match probability". This probability was calculated using neighboring particles and some heuristics based on maximum velocities and quasi-rigidity conditions over small areas of the flow. While the approach

Published online: 12 August 2012

significantly improved over nearest-neighbor approaches, it was still limited to fairly low gradient flows. Around the same time, super resolution methods were introduced (Keane et al. 1995) based on the autocorrelation of double-pulse PIV images to guide the particle matching routine. This method was augmented with the use of Kalman filter prediction by Takehara et al. (2000), which increased the robustness of the super resolution method. Cowen and Monismith (1997) introduced a technique known as hybrid particle tracking, which used the results from two-frame PIV analysis to guide the particle tracking process. Upon initially obtaining PIV results, the algorithm then used these results as a guide to search specific areas in the second image for a single particle, which was then considered the match to the particle from the first frame. It essentially constituted a modified nearest-neighbor search, using the added knowledge of approximate displacements from PIV. Further advancements along this line were made by Kim and Lee (2002) by combining the hybrid PIV–PTV idea with the match probability concept. Such an approach allowed variations in the maximum velocity along with variable rigidity conditions depending on the local flow properties, thus expanding the range of the match probability algorithm.

In recent years, other methods have been developed. One is the deterministic annealing approach (Stellmacher and Obermayer 2000) that attempts to minimize a cost function relating the particle displacements and an assumed transformation function operating between the two frames. Another is the feature tracking method based on Delaunay Tessellations (Song et al. 1999), which matches triangles rather than individual particles, taking advantage of the fact that 2-D shapes are identifiable while points are not. Other recently improved algorithms include the variational approach of Ruhnau et al. (2005), which finds the vector field as a whole rather than resolve individual vectors, and thus satisfies a minimization problem while including known smoothness properties of the flow. Mikheev and Zubtsov (2008) modified the original PTV method of Uemura et al. (1989) by taking into account the particle size when determining matches, and dubbed the method enhanced PTV (EPTV). Another method, originally developed for 3-D flows (Ponchaut 2005; Ponchaut and Mouton 2005), involves forming a first guess of the velocity field based on a weighted average between a correlation technique and a simple particle tracking technique. Appropriate weights are assigned to these vectors so that the correlation approach has more influence where it is more accurate (i.e, where the particle image density is high) and the simple particle tracking has more influence where the density is low. Finally, particle tracking uses this hybrid velocity field to create local criteria for the velocity vectors. Brevis et al. (2011) proposed an integrated cross-correlation/relaxation algorithm. The combined algorithm first uses a cross-correlation process to obtain an initial solution and further refined the results by the relaxation algorithms in the zones where the cross-correlation scheme shows low reliability. The performance of both of the individual and the integrated algorithms is compared and analyzed using synthetic and experimental images. The results show improved overall performance by the integrated algorithm at high velocity gradient and heterogeneous seeding cases. Panday et al. (2011) proposed an ant colony optimization algorithm for matching image pairs of stereo PIV images. Although the tracking algorithm could potentially be used for tracking image pairs over time, it is used to match stereo image pairs from the two camera views instead of temporal tracking. Shindler et al. (2011) proposed a PTV technique based on a modified polar coordinate system similarity method (PCSS) for tracking. The enhanced algorithm shows improved performance for cases that have inhomogeneous seeding density distributions.

One of the advantages PTV has over PIV technique is the sensitivity to high velocity gradient. While PIV has advanced to a very robust and accurate level, there is still the issue of spatial resolution. With advanced weighted iterative techniques, it has been shown that spatial wavelengths as small as twice the grid node distance are detectable (Nogueira et al. 2005). In this study, they also found that the error associated with wavelengths of this size approaches 100 %. For errors on the order of 10 %, the smallest wavelengths detectable are larger by a factor of 4–8. On the other hand, PTV is only limited by the mean spacing of particles (which goes as the square root of particle image density, defined as the number of particles per image area in pixels squared). In addition, PIV suffers from an inherent averaging effect over the area of the interrogation windows, which decreases the maximum velocity gradients that can be measured (Scarano 2003). PTV does not result in this severe averaging effect, since individual particles are tracked. With kriging interpolation (Gunes et al. 2006), it is possible to reconstruct accurate velocity gradients on a uniform grid basis from nongrid PTV results.

Comparing to PIV algorithms that analyze cluster of particle images in each interrogation window, the performance of a particle tracking algorithm depends on their ability to identify particles. In most macroscale experiments, it has been shown that the optimized particle image size for either PIV or PTV is about 2–4 pixels in diameter. For microscale studies, due to the restrictions of volumetric illumination and high magnification, the particle image size can be significantly larger. To fully utilize the high spatial resolution feature of the PTV approach, the particle density in the imaging area should be as high as possible. Thus, overlapping particles become an important issue when

identifying particle locations. One popular approach to resolving this issue is to start from a local intensity maximum and apply a Gaussian fit to locate the peak with sub-pixel accuracy. Both Gaussian surface fits and Gaussian line fits (Cowen and Monismith 1997; Marxen et al. 2000; Ohmi and Li 2000; Mikheev and Zubtsov 2008; Brady et al. 2009) have been used. Specifically, Marxen et al. (2000) found that Gaussian line fits performed as well as a surface fit with much lower computational time provided the image noise was low. A dynamic threshold binarization method proposed by Ohmi and Li (2000) and modified by Mikheev and Zubtsov (2008) provides a way to overcome the variations due to particle sizes and background noise level while preserving most of the particle images. In the case of high image noise, the Gaussian surface fit performed better, at the cost of longer computational time. Brady et al. (2009) proposed an improved 4-point Gaussian estimator that reduces the error of traditional 3-point Gaussian fit by accounting for pixel discretization effects using integral formulations. Approaches including the use of the CLEAN algorithm (Stellmacher and Obermayer 2000) and a Gaussian mask correlation (Takehara and Etoh 1999; Saga et al. 2003) apply a "model image" of the particles to the original image to find the maximum of convolution or cross-correlation, thus determining the peak location. The performance of particle mask correlation method (PMCM) tested by Takehara and Etoh (1999) shows that it is possible to use a fixed size of the particle mask for finding a range of particle sizes, and that the normalized critical distance to separately identify two particles is about unity for identical particles but increases when the intensity difference increases. Shindler et al. (2011) proposed a new feature-based particle identification method based on an optical flow equation. Instead of the intensity peak of a particle image, the barycenter of a feature is used as the location of the tracer.

The general assumption for most peak finding algorithms is that each particle results in one peak of a particle image and the intensity distribution can be approximated by a 2-D Gaussian function (Adrian and Yao 1985). Thus, a 1- or 2-D Gaussian fit can be applied to the pixels in the vicinity of a local intensity maximum to locate the particle center. As pointed out by Ponchaut (2005), this assumption no longer holds when the particles severely overlap. Marxen et al. (2000) performed simulations of overlapping particles with least-square surface fits and 3-point line fits based on this assumption, and the results showed a steep rise in the errors when the particle separation distance approaches the particle diameter. The summation of multiple particle images can result in fewer peaks, where these peaks deviate from the particles' true locations. Even if the peak number is the same as the particle number, the Gaussian fit based on the single particle assumption could lead to greater location errors since the overlap region will add bias error to the peak location toward the nearby particle. The PMCM can resolve the two overlapping particles up to a minimum critical separation distance, thus providing a way to estimate the presence of nearby particles. However, this critical distance is still larger than the particle separation distance that would cause two particles to sufficiently merge so that they would form a single peak, and it increases even more when the intensity differences between particles increase. The cascade correlation method (Angarita-Jaimes et al. 2009) suggests that instead of applying the cross-correlation once with the particle mask image, a cascade of cross-correlation operations makes the correlation peak narrower, thus decreasing the critical distance. Their simulation data show a significant improvement when compared with the PMCM algorithm, reducing the critical distance to below Rayleigh's resolution limit. The particle location is then determined by performing a 5-point 2-D Gaussian fit to find the peak location in the cross-correlation plane. The CCM algorithm provides an efficient way to separate overlapping particles and is easy to implement. However, the peak locations found from the correlation image plane may suffer additional errors. The peaks in the correlation image can be distorted due to noise, and the sub-pixel peak-fitting algorithms may introduce bias errors toward integer values due to discretization of the particle images. A well-known example is the peak-locking error encountered in typical PIV applications (Nogueira et al. 2001a, b; Liao and Cowen 2005).

In the present work, a novel and robust particle tracking technique is proposed to improve the overlap particle identification and tracking performance. The ideas of Scott and Longuet-Higgins (1991) used to solve the problem of visual correspondence have been adapted and modified to fit the concept of particle matching and to create a robust tracking algorithm. This technique and its implementation are described in Sect. 2. A modified particle identification method, based on a mixed algorithm of cascade cross-correlation method (CCM, proposed by Angarita-Jaimes et al. 2009) and Gaussian surface fitting, is developed to improve the accuracy of particle identification for overlapping particles, which is discussed in Sect. 3. The synthetic images and experimental results are discussed in Sect. 4. Finally, the conclusions are presented in Sect. 5.

2 Algorithms

2.1 Vision-based feature association

A long-standing problem in the field of computer vision has been the ability to correlate features in images, such as sequential images in time, to discern motion. In many situations, the features in the images can be very distinct,

making the problem fairly easy to solve. In some situations, however, the corresponding features may be too similar in appearance (such as particle images) to allow simple matching. In the field of computer vision, the attempt to match many similar features has led to two principles known as the "principle of proximity," and the "principle of exclusion" (Scott and Longuet-Higgins 1991). The proximity principle states that a shorter-distance feature match is more likely than a long-distance match. This reduces to the nearest-neighbor approach taken early on in the evolution of particle tracking algorithms. The exclusion principle eliminates the possibility of several features in one frame corresponding to a single feature in another frame. Together, these principles make up much of what determines a match to human vision. While other works have been proposed require the exclusion principle to be applied explicitly (Ullman 1979), Scott and Longuet-Higgins determined that conditions placed on the problem statement can enforce this principle without explicitly programming for it. The approach of Scott and Longuet-Higgins was to first develop the proximity matrix, G,

$$G_{ij} = e^{-r_{ij}^2/2\sigma^2} \tag{1}$$

where r_{ij} represents the distance between features I_i and J_j, where I and J refer to the first and second images, respectively, and the subscripts i and j are the feature indices. In the exponential denominator, σ is a characteristic distance.

Given the above proximity matrix, the next task is to determine a pairing matrix, P that maximizes the inner product, $P : \mathrm{G} = \mathrm{trace}\,(P^T G)$. The method taken by Scott and Longuet-Higgins is to find the singular value decomposition (SVD) of G, such that

$$G = TDU \tag{2}$$

By the nature of the SVD, T and U are orthogonal matrices. The entries of the D matrix (which is purely diagonal) can be replaced with ones, resulting in the identity matrix, I. Substituting this for the D matrix results in the pairing matrix P,

$$P = TIU. \tag{3}$$

This can be shown to be the matrix with the maximum inner product with the proximity matrix, having rows which are mutually orthogonal. An element of P_{ij} can be thought of as the measure of correspondence between features I_i and J_j. A large value of P_{ij} indicates a large element of G_{ij}, which is a Gaussian weighted distance, and therefore, P_{ij} provides an overall least-squared distance mapping between features I_i and J_j. This provides the principle of proximity. The orthogonality of P means there can be only one maximum element per row or per column and thus insures one-to-one mapping between particles in different images. This provides the principle of exclusion. Therefore, if an entry of the pairing matrix, P_{ij}, is the maximum value of both the row i and the column j, then features I_i and J_j are considered matches. Further mathematical details can be found in Scott and Longuet-Higgins (1991) and Schonemann (1966).

This technique clearly has applications in the field of particle matching where both the principle of proximity and the principle of exclusion play major roles. Also, the method is very simple to implement once the particle locations are known as it only requires a SVD, matrix multiplication, and a maximum value search. However, there are significant problems associated with this technique when considering its use for particle tracking. The first issue concerns particle losses, or unmatchable features, due to in-plane losses, out-of-plane losses, or misidentification of particles. These so-called rogue points can corrupt the matching results. The second major problem is that the algorithm requires, as an input, a single characteristic length on which to base the proximity matrix.

Another known problem of the Scott and Longuet-Higgins method is the inability to match particles that travel through a large rotation between frames. This clearly has implications in the field of PTV, especially in studying vortical flows. However, as noted in Luo and Hancock (2002), the critical angle is on the order of 20°. While this is a limiting factor in some applications, PTV rotation levels should never be as high as 20° if the experiment is properly performed. Based on the Scott and Longuet-Higgins method, a modified method by Pilu (1997) is proposed to improve the matching results. The similarity between features is taken into account together with the proximity and exclusion principles. This produces a much more selective pairing matrix. This is done by calculating the normalized cross-correlation coefficient C_{ij} of the feature pair:

$$C_{ij} = \frac{\sum_{u=1}^{W}\sum_{v=1}^{W}\left(I_A(u,v) - \bar{I}_A\right)\cdot\left(I_B(u,v) - \bar{I}_B\right)}{W^2 \cdot \sum\left(I_A\right)\cdot\sum\left(I_B\right)} \tag{4}$$

where $\bar{I}_A$, $\bar{I}_B$ are the average, and $\sum(I_A)$, $\sum(I_B)$ are the standard deviation of all pixel intensities of the $W \times W$ subwindow area I_A and I_B, each centered on feature i and j, respectively. C_{ij} varies from -1, for completely uncorrelated matches, to 1 for identical matches. Therefore, a new proximity matrix G'_{ij} can be defined as follows:

$$G'_{ij} = G \cdot e^{-(C_{ij}-1)^2/2\gamma^2} \tag{5}$$

The new term added to the original proximity matrix is a Gaussian weighted correlation coefficient, in which γ is a factor to control the speed of decay of the weighting of the

similarity term that is set to 0.4 per Pilu (1997). The range of C_{ij} is from -1 to 1, so the new proximity matrix G' still ranges from 0 to 1, and the principle of proximity is maintained since G_{ij} is larger when the features i and j are closer, or the correlation value C_{ij} is larger. This modified algorithm greatly improves the ability of the method to deal with rogue points, producing more valid matches than the original method.

In the original Scott and Longuet-Higgins method, the choice of σ is arbitrary, but is suggested to reflect the average displacement of the features. Based on the experimental results, Pilu (1997) suggests that σ should roughly match the actual displacement. For implementation of PTV, it is a natural choice to use PIV results as a guide. Since PIV results are still a regional average over a certain interrogation window size, data interpolation is used to provide more accurate estimate of the local σ value.

The tracking algorithm proposed in this paper is based on the original Scott and Longuet-Higgins (1991) method, with the modification made by Pilu (1997). The implementation of the method is hybridized with PIV results, and an iterative scheme with outlier detection (Duncan et al. 2010) is used to increase the robustness and accuracy of the method. The details of the implementation are discussed in Sect. 3.2.

$$R_1(u,v) = \frac{\sum_{i=u-m/2}^{u+m/2}\sum_{j=v-n/2}^{v+n/2}\left(I(i,j)-\bar{I}\right)\left(I_M(i,j)-\bar{I}_M\right)}{\sqrt{\sum_{i=u-m/2}^{u+m/2}\sum_{j=v-n/2}^{v+n/2}\left(I(i,j)-\bar{I}\right)^2}\sqrt{\sum_{i=u-m/2}^{u+m/2}\sum_{j=v-n/2}^{v+n/2}\left(\bar{I}_M(i,j)-\bar{I}_M\right)^2}} \tag{9}$$

2.2 Particle location identification

Based on CCM algorithm, an improved algorithm is proposed here to fully utilize the advantage of the CCM algorithm and avoid the potential error discussed above. Each PTV image can be considered as a summation of an unknown number N of particle images, each having a different location, intensity and radius assuming a Gaussian shape distribution, plus the noise signal mainly due to thermal noise of the CCD sensor. Thus, the intensity $I(j, k)$ at pixel (j, k) is

$$I(j,k) = \sum_{i=1}^{N}(I_0)_i \cdot e^{\frac{X_i(j,k)^2}{2r_i^2}} \tag{6}$$

where $(I_0)_i$ is the peak intensity of the ith particle image, $X_i(j, k)$ is the distance from the pixel to the particle center (x_{ci}, y_{ci}), and r_i is the representative radius of the particle image. The particle identification process finds a solution

$$I'^{(j,k)} = \sum_{i=1}^{N}(I_0')_i \cdot e^{\frac{X_i(j,k)^2}{2r_i'^2}} \tag{7}$$

so that the difference between $I(j, k)$ and $I'(j, k)$ for all pixels in the image is minimized in a least-square sense. Note that the number of particles, N, in traditional particle identification algorithms is assumed to be equal to the number of peaks in the image, and $I(j, k)$ is independent for each particle i under the assumption that the particle image density is sufficiently low. Thus, for each particle i, the equation can be reduced to

$$I_i(j,k) = I_i e^{\frac{X_i'(j,k)^2}{2r_i'^2}} \tag{8}$$

in order to make the 3- or 5-point Gaussian fit work. Therefore, with overlapping particles, the key is to estimate N as accurately as possible. Since the CCM algorithm provides a way to separate the overlapping particle peaks, N can be estimated by counting the number of peaks in the last cross-correlation image from the CCM algorithm. The CCM algorithm first calculates the cross-correlation image R_1 between the original particle image I and the model particle mask image I_M, where the model particle mask image is defined as an intensity image of size $m \times n$ containing a particle image with a Gaussian shaped intensity profile which follows Eq. (8). The operation is then repeated to generate a cascade correlation image R_2 by replacing I in Eq. (9) with correlation image R_1 and reducing the particle mask image radius r by 1 pixel. In the original CCM algorithm, the peak locations in the R_2 plane are used to indicate the particle locations. In the present method, the number of peaks, N, is counted instead. With the Nin Eq. (6) known, the least-square fitting can be performed to find the best estimate of the particle locations in the original image I. This modification eliminates errors produced during the cross-correlation operation, such as the peak-locking effect.

3 Implementation

3.1 Modified CCM algorithm

In practice, the computational cost of this method for a typical PTV image containing thousands of particles is high. The intensity of each particle considered only extends to $\pm 4\ r_i$ due to the e^{-2} intensity level drop of the Gaussian curve. This indicates that the image can be broken into small sections to reduce the computational cost without sacrificing accuracy. The raw image is broken down into small blob images, each containing an unknown number of particles. A blob is defined as a set of connected pixels. As an example, in Fig. 1, the binary image contains three blobs. The blob identification process starts here with Otsu's method (Otsu 1979), which segments the foreground (blobs) and background image (noise) by finding the threshold to minimize the variance between the two classes of pixels. The connected foreground pixels are then sorted into blobs. Each of the blobs is then considered as an independent image containing an unknown number of particles described by Eq. (6). The number of particles in each blob is then determined by the improved CCM algorithm described in the paragraph below.

Expanding the original idea of the CCM method, the cross-correlation operation in Eq. (9) is now performed k times, with a gradually decreasing particle mask size. Each time a cross-correlation is performed, the particle mask size (the representative radius r) shrinks by 1 pixel until it reaches a user determined minimum radius. This modification has two purposes: one is to reduce the critical separation distance between particles even further since the correlation is narrower. The other goal is to increase the ability to detect a wider range of particles, since the results from Takehara and Etoh (1999) show that the correlation coefficients drop much more quickly when the particle size is smaller. Thus, a sweep of radius from large to small provides more chances to detect the heavily overlapped small particles. The number of peaks N is calculated by counting the local maximain the last correlation plane R_k which are greater than a threshold value. Once the number of particles N is estimated, a nonlinear least-square fit is performed by minimizing χ^2:

$$\chi^2 = \sum_{j=1,j=1}^{j=m,k=n} \left[I(j,k) - \sum_{i=1}^{N} (I_0)_i \cdot e^{\frac{X_i(j,k)^2}{2r_i'^2}} \right]^2 \quad (10)$$

By solving the least-square fit problem, the location (x_i, y_i), intensity $(I_0)_i$, and radius r_i of each of the particles in the blob can be found. This process is repeated for all the blobs, and the final result is the summation of all the blob results. The block diagram for the whole procedure is shown in Fig. 2.

To verify the performance and robustness of the new method, simulation tests are carried out on images of two identical overlapped particles, which are together varied in size, normalized separation distance, and noise types. Each of the simulated particle images is generated using the Gaussian intensity profile defined by Eq. (8), with fixed I, x_c, y_c, and r. The simulated particle diameter, D, varies from 4 to 20 pixels, is defined as the e^{-2} intensity level of the Gaussian. D is equal to $4r_P$, which is the representative radius of the particle image. The particle overlap ratio is defined as $(D - L)/D$, where L is the separation distance between the overlapped particles and D is the particle diameter. The particle overlap ratio in the present tests

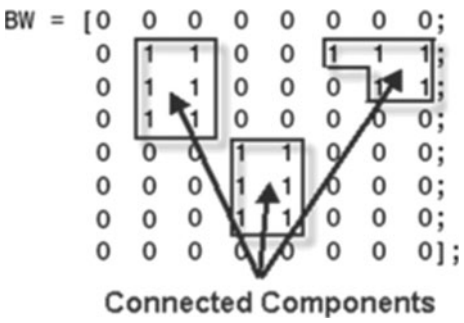

Fig. 1 Example of connected pixels forming blobs in a binary image (reproduced from MATLAB®)

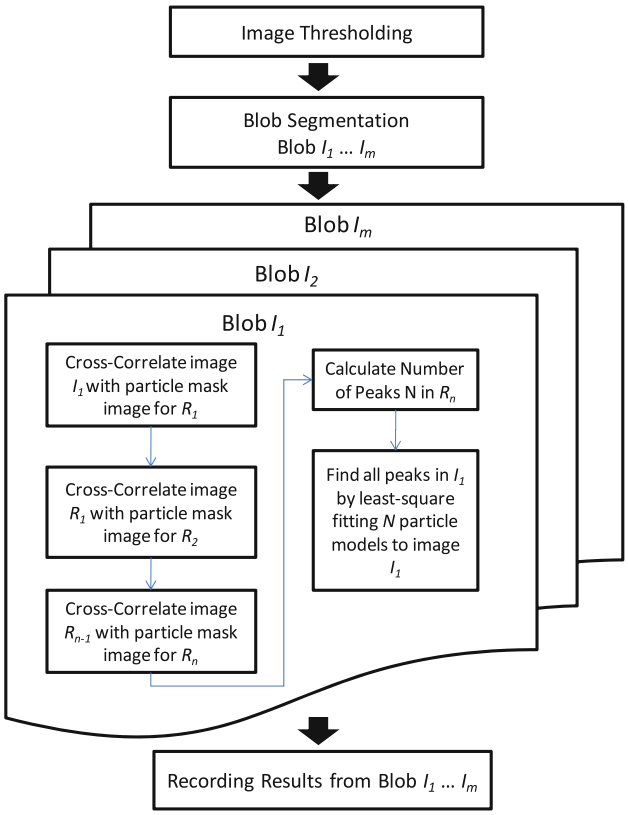

Fig. 2 Process flow of the proposed particle identification algorithm

varies from −150 to 50 %. The pixel intensities are then the sum of the two particle images discretized by sampling the Gaussian intensity profile. Two types of noise are tested: the Poisson noise and Gaussian noise. The Poisson noise is used to simulate photon noise, which is the dominant noise source of fluorescence microscopy encountered in micro-PIV applications. The noise of each pixel follows a Poisson distribution with a mean that is equal to the intensity value $I(i, j)$ of the pixel (i, j). Since the noise increases as $\sqrt{I(i,j)}$, the signal to noise ratio (SNR) can be calculated as $\text{SNR} = I_c/\sqrt{I_c} = \sqrt{I_c}$, where I_c is the intensity value at the particle image center. The Poisson noise is added so that the signal-to-noise ratio varies from 10 to 25. The Gaussian noise is used to simulate the thermal noise of an image sensor, which is a major noise source in general PIV applications. The Gaussian noise tested in this paper is added with a standard deviation of 2.5 and 5 % of the dynamic range of the model sensor, which is set to 8 bits (0–255). The test for each case is repeated 1,000 times, and the averaged results are reported.

Figure 3 shows the relationship between the separation distances of two identical particles at different noise levels, processed by the proposed method with $D = 20$ ($r_P = 5$). Figure 3a shows the results of the Poisson noise level variation from no noise (SNR = infinity) to SNR = 10, and these results are compared to the results of the original CCM algorithm (Angarita-Jaimes et al. 2009). All the averaged errors of the current method are below 0.2 pixels, with an increasing trend when the overlap ratio increases beyond 0 %. Compared with the original CCM algorithm, the error increases to 0.154 pixels when the particle overlap ratio reaches 50 % for the case of SNR = 10, whereas the original CCM method's error increases beyond 0.5 pixels. Figure 3b shows the results of different Gaussian noise level. They show similar trends as the Poisson noise tests. For a 50 % particle overlap ratio, the errors are within 0.25 pixels, and errors are within 0.09 pixels for all overlap ratios under 40 %.

Figure 4 shows the effects of particle size and Gaussian noise level on the particle location errors. The particle sizes vary from $D = 4$ to $D = 20$ and different particle overlap ratios varying from 0 to 50 % are shown in different curves. In Fig. 4a, the Gaussian noise level is 2.5 %, and at high overlap ratios, the current algorithm fails to resolve the overlapping particles when $D < 10$, thus causing the loss of data points at each curve. As particle size increases, the maximum resolvable overlap ratio increases up to 50 %. This result is expected, since the CCM method requires enough particle image spatial resolution to form the individual correlation peaks. In Fig. 4b, the noise level is 5 %. For larger particle sizes ($D > 6$), the proposed method is able to separate the overlapping particles with pixel errors below 0.1 for overlap ratios of up to 40 %. For 50 % overlap, the resolvable particle size range is the same, and the errors go up to 0.15 pixels due to the increase in noise level. For small particles, the error comes from the background pixels. Since the particle size is smaller, more pixels containing only noise contribute to the total error of the least-square fitting.

In practice, the size of seeding particles varies if polydisperse particles are used. Even if the seeding particles are uniform in size, the particle image diameters can still vary due to the out-of-focus effect of the optical system. Furthermore, the laser light sheet has a Gaussian cross section; thus, monodisperse particles image with an optical system within the depth of field will still see a variation due to the light sheet intensity variation and the position of particles within the sheet. Fig. 5 shows the performance of the proposed method with two particles of different sizes overlapping at different Gaussian noise levels.

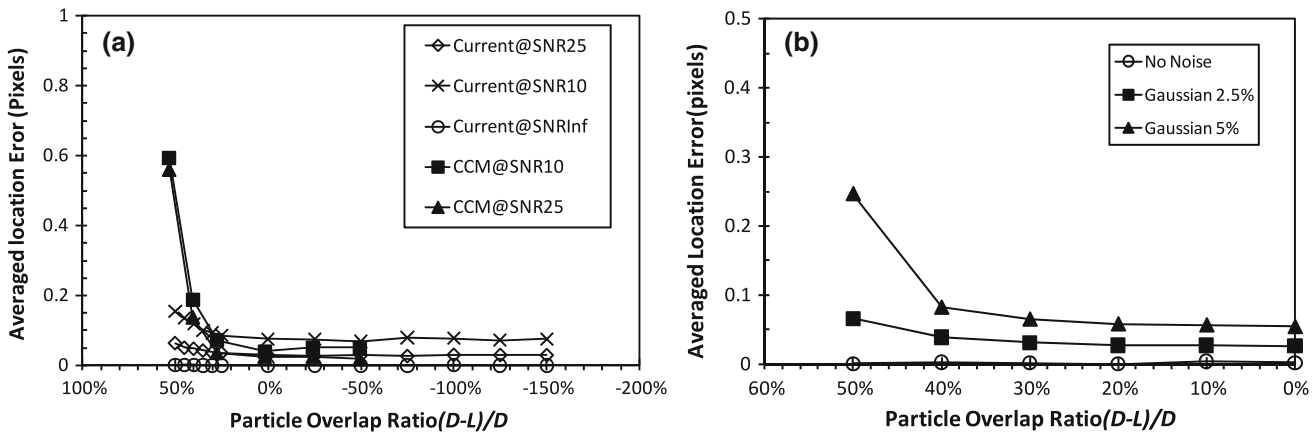

Fig. 3 Averaged particle location error versus particle overlap ratio between two particles for **a** Poisson noise levels at infinity, 25 and 10. **b** Gaussian noise levels at 2.5 and 5 %

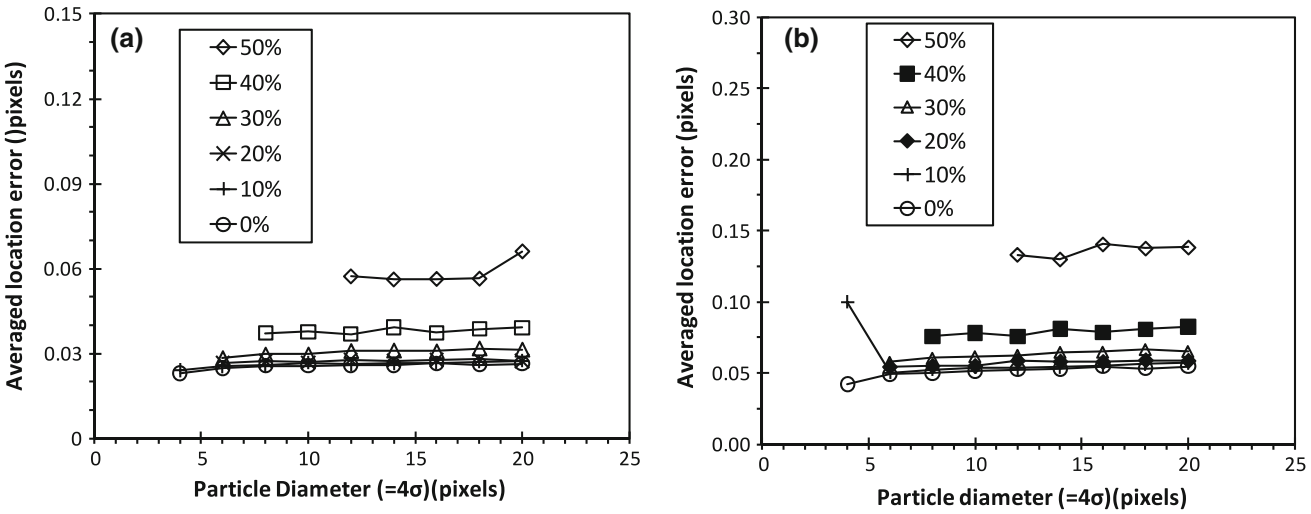

Fig. 4 Averaged particle location error versus particle diameter for different overlap ratios **a** 2.5 % Gaussian noise, **b** 5 % Gaussian noise

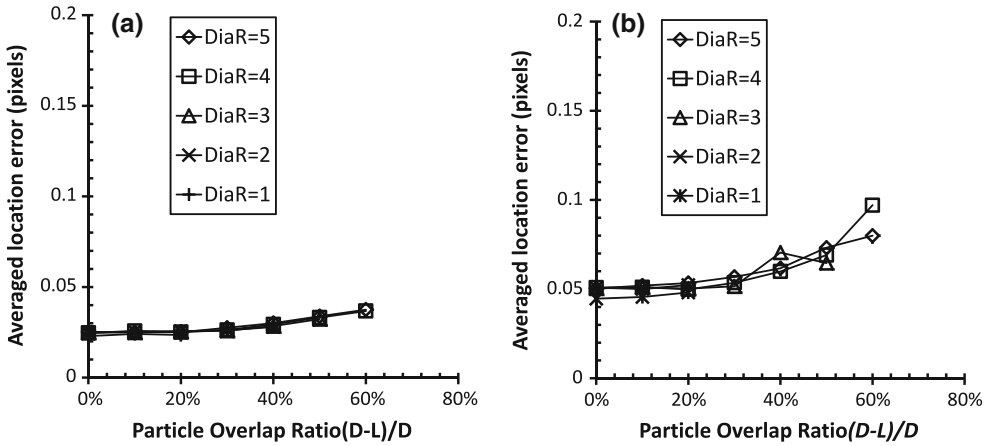

Fig. 5 Averaged particle location error with various particle diameter ratios and noise levels. **a** 2.5 % Gaussian noise versus particle overlap ratio. **b** 5 % Gaussian noise versus particle overlap ratio

The sizes of two particles are controlled by the particle diameter ratio, DiaR. In this test, the smaller particle is fixed to 4 pixels in diameter, while DiaR varies from 1 to 5. The particle diameter D used here is the average of the two particles. The detectable overlap ratio limit rises to 60 % when DiaR is 4 or 5. This is due to the fact that the proposed method separates overlap particles better with larger particle diameter ratios. For DiaR smaller than 4 at 60 % overlap, the algorithm cannot resolve the overlap; thus, no data points are shown. The errors are under 0.1 pixels with overlap ratios of up to 60 %, and for overlap ratios under 50 % the errors are lower than 0.07 pixels. The error increases slightly for larger overlap ratios but insensitive to DiaR changes. It is clear that the error increases as the Gaussian noise level increases, and the algorithm begins to fail to resolve both particles at all overlap ratios above 50 % at a 5 % Gaussian noise level. The error for DiaR $= 4$ at 60 % overlap is slightly larger than DiaR $= 5$. This is again due to the fact that the distance between the peaks for the smaller particle is actually larger for the same overlap ratio as the DiaR increases.

3.2 Modified vision matching

With both PIV data and particle locations obtained, the particle matching algorithm can be implemented. To account for the different characteristic displacements present in the flow, twice the displacement magnitude at each particle location (found by interpolating the PIV results) is used as the characteristic displacement σ. The choice of the σ value is based on the finding that the tracking performance is better when σ is an overestimate of the true displacement [see section 5 of Scott and Longuet-Higgins (1991)]. This displacement is then used to construct the proximity matrix discussed above, which is then processed via SVD to determine a pairing matrix. Each entry, which is the maximum of its row and column, is considered a match and is subject to validation.

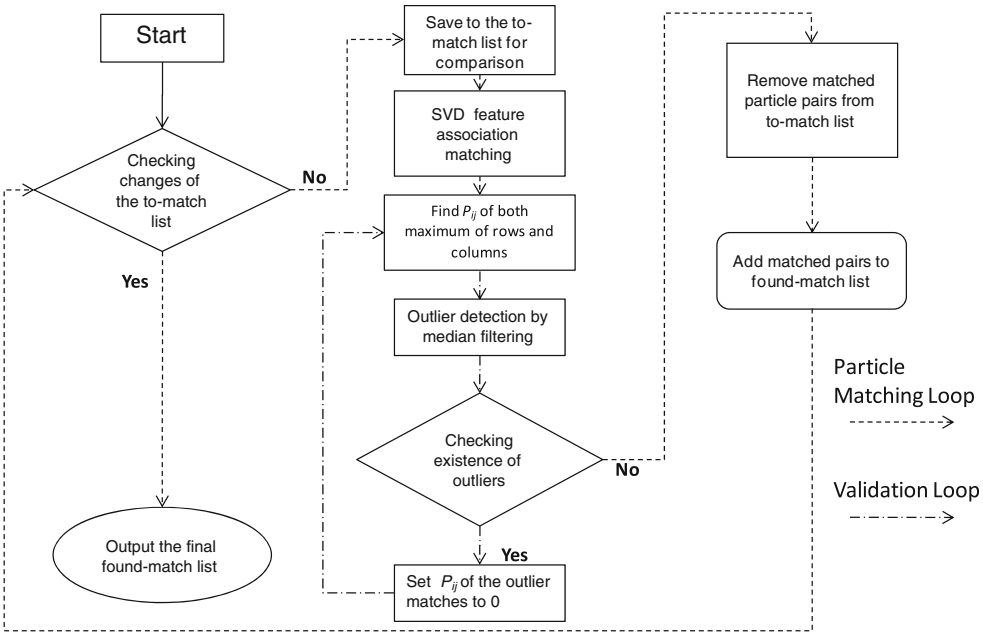

Fig. 6 Process flow of the proposed tracking algorithm

In order to make the feature matching technique described in Sect. 2.1 more robust, two iterative approaches are taken. The outer iteration, termed the particle removal loop, focuses on removing already matched particles from the possible matches list. In this manner, straightforward matches are made early on in the process, making the remaining particle list easier to match later on. This iteration is in accordance with the exclusion principle, since any particle found to be a match in an early iteration can clearly not be a match with another particle in future iterations. The second iterative loop, termed the validation loop, takes place inside the particle removal loop listed above. For each particle list, the P matrix is created (by way of the SVD of the modified proximity matrix G' mentioned in Sect. 2.1) and maxima of both rows and columns are sought. When such a maximum is found, an outlier detection step is performed using the modified universal outlier detection method (Duncan et al. 2010). If the entry in the P matrix is considered an outlier, then it is set to zero. Upon the next iteration of the validation loop, another entry in the P matrix may become the maximum of its row and column since the previous maximum may have been removed. This loop ends when the P matrix no longer changes, at which point the particle removal loop moves on to the next iteration until completion (Fig. 6).

Since computational times are always of concern, some approaches are taken to reduce the load to more reasonable levels. It was found that breaking an image into smaller windows results in significantly less computational effort while retaining accuracy when the results are recombined. Table 1 shows the PTV results from breaking a 512 × 512 image down into overlapping interrogation windows, where a Dell Precision PWS490 Intel® Xeon® CPU E5345 @2.33 GHz with 16.00 GB of RAM was used for these calculations. As the particle image density increases from 0.01 to 0.06, the computational time required to complete particle tracking goes from $O(n)$ to $O(n^2)$ where n is the side length of each interrogation window, as shown in Fig. 7. At the highest density, the computational cost drops from over 14 h down to 14 min, with a loss of only 12 matches out of more than 15,000 by using a 64 × 64 interrogation window rather than analyzing the full image all at once. These modest losses are caused by the sensitivity of the SVD method to outliers, which inevitably exist due to unmatchable particles around the edges of an image or interrogation window. In the interest of maintaining accuracy while reducing computation time, all PTV runs recorded in Sect. 4 use 64 × 64 or 128 × 128 pixel interrogation windows overlapped by 50 %.

Table 1 Effect on PTV results from breaking 512 × 512 images with different particle image densities into overlapping windows

Window size	64 × 64	128 × 128	256 × 256	512 × 512	Total no. of particles
Matches (0.01)	2,592	2,592	2,592	2,592	2,611
Matches (0.03)	7,828	7,828	7,829	7,829	7,879
Matches (0.06)	15,384	15,395	15,397	15,396	15,512

4 Experimental results of synthetic images

4.1 Generation of synthetic images

To test the particle matching capability of the algorithm, the algorithm is first applied to simulated flows with known

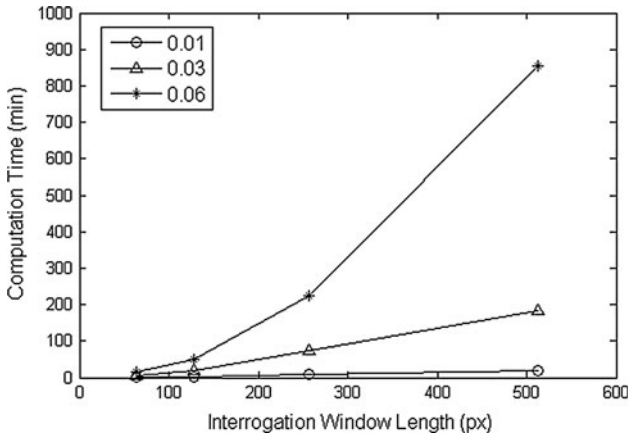

Fig. 7 Computational time versus interrogation window length at varying particle image densities

particle locations. Four parameters of each tracer particle are generated: the peak intensity I, representative radius σ, and the peak location (x_c, y_c). The location is always randomly generated, and the intensity and radius are either fixed or randomly generated depending on the experimental condition. The peak locations in the first image are generated in a 512 × 512 image region, and then, peak locations for the second particle image are calculated using the simulated flow field. These form the particle lists for the known particle location tests discussed in Sect. 4.2. Each particle image is then generated in the same way as the particle overlap test presented in Sect. 3.1. The intensities at each pixel are summed from all the particles that occupy the same pixel to form the test images. The formation of the image in this manner is based on the assumption that particle image is not only formed by direct illumination but also due to fractions of light scattered from other particles (Raffel et al. 1998). A detailed discussion of the validation of this assumption is in Sect. 4.5. Since the proposed tracking method is mainly based on point-set matching and the simulated flow is assumed to be 2-D, the variation of intensities between image pairs is assumed to be zero.

The particle image density, previously defined as the number of particles per image area, varies from 0.01 to 0.06. Since the proposed tracking algorithm is mainly based on matching particle locations between 2-D image frames, the particle image density is a more appropriate measure of the performance than the actual particle seeding density. One of the concerns when using a high particle image density is the possibility of two-phase flow effects or particles interacting with the flow and changing the flow characteristics. Under a typical experimental condition with laser light sheet thickness of 1 mm, tracer particle diameters of 10 μm, an image area of 100 × 100 mm^2, and a 256 × 256 pixel particle image density of 0.06, the volume fraction Φ_p of particles is 2.09×10^{-7}. Based on the results shown in Figure 1 in Elghobashi (1994), effects on turbulence for these conditions are negligible. Thus, the particle image density range in the current tests is free from the two-phase flow effect.

4.2 PTV results from moving wall images

A moving wall (Stokes' first problem) synthetic flow is chosen to verify the algorithm. All the image sizes are 512 × 512 pixels. The PTV algorithm is guided by PIV results, which are obtained by processing sequential images, with window-shifting and multi-passes resulting in 16 × 16 pixel interrogation windows with 50 % overlap, and application of an outlier removal algorithm (Duncan et al. 2010).

In order to quantify the accuracy of the new method, two parameters suggested by Ruhnau et al. (2005) are used. These are the yield and reliability, both given as percentages. The yield (E_Y) is defined as the number of correct vectors found by the tracking algorithm (n) divided by the total number of particle pairs between the frames (v). The reliability (E_R) is defined as n divided by the total number of vectors (correct and incorrect) identified by the tracking algorithm (d):

$$E_Y = \frac{n}{v} \tag{11}$$

$$E_R = \frac{n}{d} \tag{12}$$

To quantify correct matches in these cases, a 1-pixel tolerance is used [EPTV: Mikheev and Zubtsov (2008), NRX: Ohmi and Li (2000), VAR: Ruhnau et al. (2005)], as well as a tighter 0.5-pixel tolerance to further quantify how well the PTV algorithm performs. In addition, the particle yield is defined as the number of particles found divided by the total number of particles within the image. Finally, RMS errors recorded in this section are a measure of the error between actual displacements found with PTV and the exact displacement from the known analytic solutions.

The synthetic images are generated using flow over a moving wall with a velocity profile described as:

$$u = U \times (1 - \mathrm{erf}(y/2\sqrt{\mu t})). \tag{13}$$

Here, $U = 10$, $\mu = 5$, and $t = 75$, with simulation results shown in Table 2. The particle image density is 0.03, and particle image diameters are 4 pixels. The parameter, t, determines the sharpness of the velocity gradient.

Table 2 shows the results from two tests. In the first, the exact particle locations are known, that is, the particle identification method is skipped, and the exact locations are fed directly into the matching algorithm.

Table 2 PTV results using exact particle locations and results from particle finding algorithm

	Particle found	Particle yield (%)	Matches found	Match yield with 1-pixel tolerance (%)	Reliability with 1-pixel tolerance (%)	Reliability with 0.5-pixels tolerance (%)	RMSE (pixels)
Known particle locations	–	–	3,638	100	99.7	99.7	Machine precision
Unknown locations	3,638	76.6	2,786	99.6	98.3	98.8	0.129

Particle image density 0.03

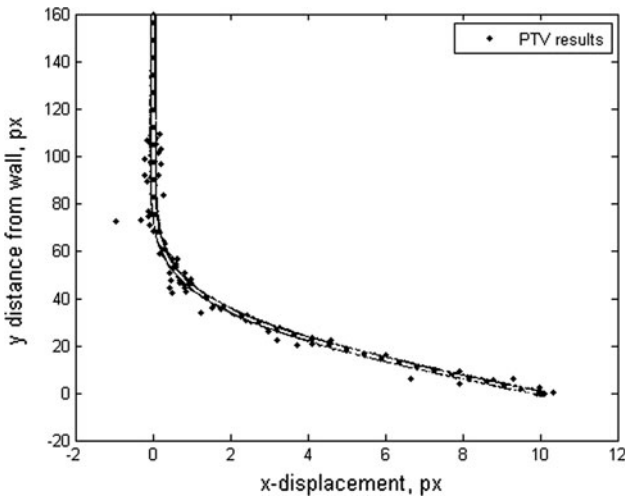

Fig. 8 PTV velocity profile for moving wall flow compared with analytic flow profile which is shown as a dashed white line superimposed on the scattered PTV data

In the second test, the particle location algorithm is used to identify particles within the test images, and then, these results are used in the matching algorithm.

It can be seen that the matching algorithm is capable of excellent accuracy so long as it has accurate particle locations. When errors due to particle location and overlapping particles are included, the displacement error rises to 0.13 pixels and the reliability drops slightly from 99.7 to 98.3 % and 98.8 % for 1- and 0.5-pixel tolerances, respectively. At this particle image density, there are a significant number of particle images overlapped beyond the range that the CCM algorithm can resolve, such that 76 % of particles within the image are identified. However, almost 99 % of the matches made between these particles are still accurate to within 0.5 pixels.

A scatter plot of PTV results from a pair of moving wall images is shown in Fig. 8. The exact analytic solution is overlaid as a solid white line. For another comparison, the scattered PTV data are fitted to Stokes' first problem, where the parameters U, μ, and t are varied to minimize the sum of squared errors between the PTV data and the fit. Of course in a real flow, the analytic solution would not be known and a suitable curve would need to be chosen to fit the data. However, this method is used in order to provide another quantification of the error of the PTV results without introducing errors from the choice of a suitable fitting curve. The results from this curve fitting were $U = 10.01$, $\mu = 5.05$, and $t = 73.67$. The R^2 value for this fit is 0.99999 and the average error of the three fitting parameters was 0.98 % when compared to the true flow parameters, which are $U = 10$, $\mu = 5$, and $t = 75$.

4.3 Error due to gradients, displacements, and PIV guidance

We wish to gain some insight into this method's performance in high gradient flows and the impact that PIV error can have on PTV results. It is known that PIV methods will underestimate displacements in the presence of a flow gradient because they examine a region of the flow in which particles with larger displacements leave the interrogation window more frequently than particles with smaller displacements. A generic PTV algorithm that examines individual particles will not suffer from these errors. The current algorithm is a hybrid of PIV and PTV, and thus, we wish to examine whether the strengths of PTV are lost because of the reliance on PIV in choosing a characteristic displacement to guide the matching algorithm. To isolate the effects of gradients on the matching algorithm, simple 1-D uniform shearing displacements with known particle locations were generated, with the resulting error, yield and reliability plotted in Fig. 9. Additionally, the PIV guidance was replaced with guidance from the exact analytic solution when calculating the characteristic displacement, σ (see Sect. 3.2). Finally, the uniform shearing region in each image existed until a maximum displacement was reached. Two different image sets were generated, one with displacements capped at ± 7 pixels and another at ± 25 pixels.

A number of conclusions can be drawn from these plots. First, the error tends to increase with increasing gradient. When displacements are kept moderate (7 pixels or less), the trend is roughly linear and the error of matches even at the highest gradient value is below 0.3 pixels.

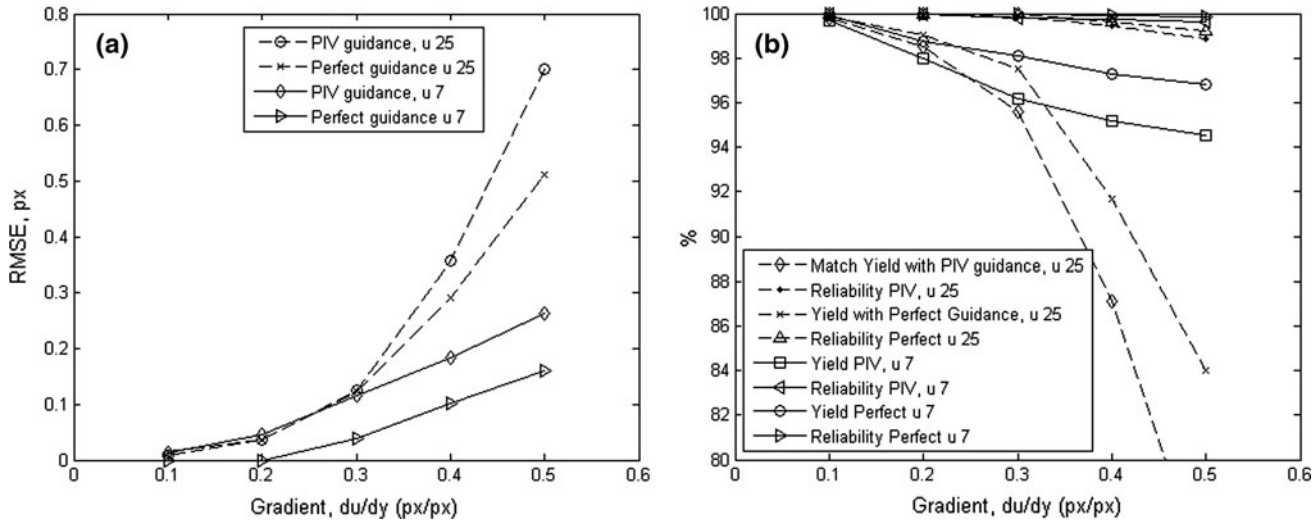

Fig. 9 **a** RMS error and **b** percent yield and reliability versus flow gradient for uniform shearing flow. Flows containing maximum displacements of ±7 and ±25 pixels are compared. The PTV matching is guided both by PIV and exact analytic solutions

Table 3 Effect of particle image density on PTV results

Particle image density	Particle found	Particle yield (%)	Matches found	Match yield with 1-pixel tolerance (%)	Reliability with 1-pixel tolerance (%)	Reliability with 0.5-pixels tolerance (%)	RMSE (pixels)
0.06	4,332	58.6	4,021	91.3	98.3	93.4	0.376
0.03	2,865	75.7	2,820	98.1	99.6	98.9	0.111
0.01	1,121	92.1	1,116	99.5	99.9	99.8	0.042

For the larger 25-pixel displacements, the error increases more rapidly, especially above 0.3 pixel/pixel gradients. Similarly, the lower displacement shearing flow experiences a modest drop in match yield compared with the 25-pixel displacement images. Finally, we can see that the use of PIV as a guide for the PTV adds error to our matching results while lowering the yield and reliability. At low gradients, the additional error is small, and at the highest gradients, PIV guidance adds between 0.1 and 0.2 pixels to the RMS error. In these tests, the PIV window dimensions were 22 × 22 pixels, using window-shifting and multi-passing routines. The reliability of matches remains at or above 99 % in all cases. To obtain the best performance from this matching algorithm, these high pixel-based gradients should be avoided when possible by reducing the time step between experimental images.

4.4 Effect of particle image density, diameter, and intensity

In order to assess the effect of particle density, simulations for particle image densities of 0.01 and 0.06 were also performed (see Table 3), showing particle yields of 92 and 59 %, respectively. Improvements in reliability, match yield, and RMS error can be seen at lower particle image densities, while the opposite is true at higher densities. This performance is a consequence of having fewer particles that are overlapped beyond the range of those shown in Fig. 4.

In order to better describe this PTV algorithm's optimum test conditions, plots of RMS error, match yield and reliability versus particle image density are shown in Fig. 10. Lower particle densities produce less error. However, more particle images are desirable to increase the velocity data resolution. A good balance for this PTV method appears to occur around a particle image density of 0.03–0.04. However, even at very high particle image densities, the reliability of matches remains above 98 %.

Since larger particle image diameters give the particle identification algorithm more data to find the exact center of each particle, it is desirable to have larger particle image diameters for particle identification algorithm to reduce the peak location error, as suggested by Mikheev and Zubtsov (2008). However, larger diameters cause more particle image overlaps beyond the range of those shown in Fig. 4, which make particle identification more difficult. Therefore, a trade-off is necessary to maximize on accurate particle identification. To determine this, a moving wall

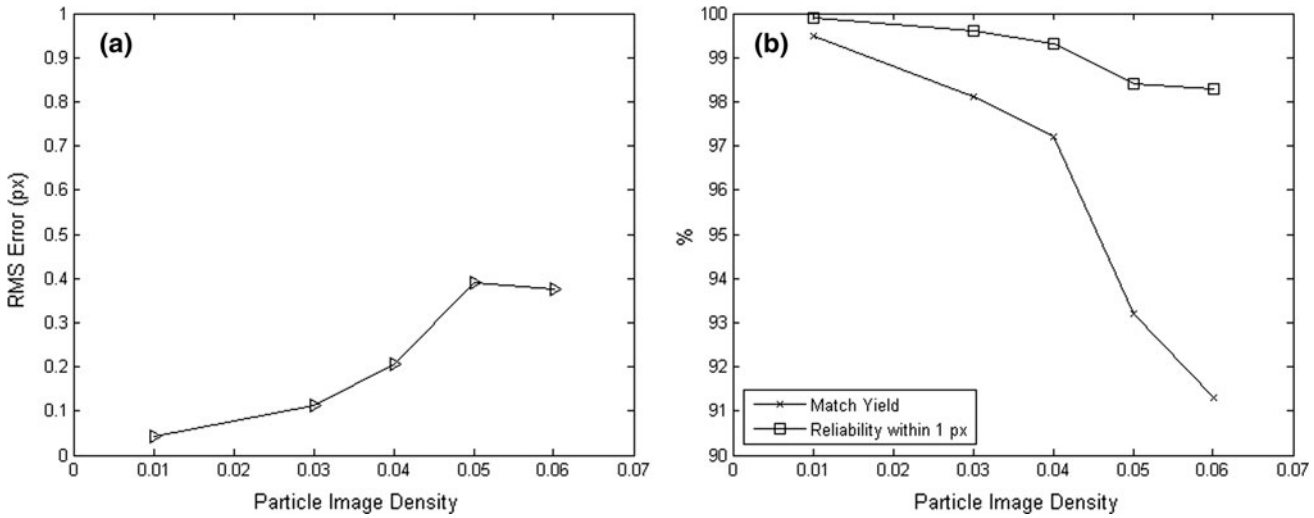

Fig. 10 **a** RMS error, **b** match yield and reliability versus particle image density

Table 4 Effect of particle image diameter and intensity on PTV results

Particle diameter	Particle found	Particle yield (%)	Matches found	Match yield with 1-pixel tolerance (%)	Reliability with 1-pixel tolerance (%)	Reliability with 0.5-pixels tolerance (%)	RMS (pixels)
4	2,865	75.7	2,820	98.1	99.6	98.9	0.112
5	2,689	71.0	2,585	94.9	98.8	95.4	0.218
7	2,412	63.7	2,090	83.5	96.3	85.9	0.391
Random intensity and diameter	2,792	73.8	2,620	92.6	98.7	93.0	0.259

flow with a particle image density of 0.03 is used to test the effect of different particle diameters, since the reliability at this density is around 99 % (see Table 3) while particles are not too sparsely distributed. Results are shown in Table 4. Reliability values within 0.5-pixels tolerance for these tests are above 95 % for 4 and 5 pixel diameters. With a 7 pixel particle diameter, the reliability with 0.5-pixels tolerance drops to 86 % due to more severe particle overlapping. Particle yield also decreases with increasing particle diameter due to more irresolvable particle overlapping. For all three cases, the PTV reliabilities with a 1-pixel tolerance are above 96 %.

In all previous synthetic images, particle images were created using a constant peak intensity (i.e., they were illuminated within a light sheet that had a top hat intensity profile). In order to more closely model experimental images, the peak intensity and diameter are randomized. The intensities are distributed about a mean of 175 with a standard deviation of 25. The diameters are distributed about a mean of 4 pixels with a standard deviation of 0.57 pixels. We can see that this randomization degrades the PTV performance and raises the error to 0.26 pixels or twice the error for uniform particle images with 4 pixel diameters. Even though the CCM algorithm can distinguish overlapped particles, it can be seen that smaller particle images are desirable for optimum performance with this PTV method.

4.5 VSJ standard PIV images

The proposed algorithm is applied to the standard PIV images from the Visualization Society of Japan (VSJ). The images used in the present work is from series #301, which is generated based on 3-D large-eddy-simulation (LES) of a two dimensional planar jet impinges on the wall (Okamoto et al. 2000). The synthetic 256 × 256 image pair contains about 4,000 particle pairs with a maximum displacement of 10 pixels. The particle images have a mean diameter of 5 pixels, and the standard deviation is 1.4 pixels. These images have been used by many other researchers (Ohmi and Li 2000; Ruhnau et al. 2005; Mikheev and Zubtsov 2008; Shindler et al. 2011; Brevis et al. 2011), so it is an ideal subject for testing and comparison purposes.

Similarly to the analytical 2-D flow tests in the previous sections, the test performed here is divided into two parts

Table 5 PTV results with known/unknown particle location and comparison to previous work of VSJ 301 image

Algorithm	Particle location	Matches possible	Matches found	Matches correct	Match yield (%)	Reliability (%)
Present work (tracking only)	Known	4,042	4,039	3,927	97.23	97.15
VAR (Ruhnau et al. 2005)	Known	4,042	4,039	3,894	96.34	96.41
EPTV (Mikheev and Zubtsov 2008)	Known	4,042	3,863	3,823	94.58	98.96
ICCRM (Brevis et al. 2011)	Known	4,042	NA	3,980	98.46	NA
Present work (particle identification + tracking)	Unknown	2,095	1,846	1,761	84.06	95.40
EPTV (Mikheev and Zubtsov 2008)	Unknown	2,029	1,759	1,733	85.41	98.52
VAR (Ruhnau et al. 2005)	Unknown	NA	872	865	NA	99.20
NRX (Ohmi and Li 2000)	Unknown	NA	808	788	NA	97.52
MF-EPS (Shindler et al. 2011)	Unknown	NA	1,160	1,146	NA	98.80
2F-EPS (Shindler et al. 2011)	Unknown	NA	1,123	1,112	NA	99.00

using known and unknown particle locations. The image pair used is image 0 and image 1 of the #301 series with 4,042 matchable pairs. In the known particle location test, out of 4,039 pairs found by the matching algorithm, 3,927 of them are correct vectors. This result gives a yield and reliability of 97.15 and 97.23 %, respectively. Since the mean diameter of the particles in the image is only 5 pixels, for the unknown particle test, the particle mask radius is set to 1 pixel. The matching algorithm parameter setting is the same as the previous tests. In the unknown particle location test, the particle identification algorithm found 2,097 and 2,095 particles from the image pair. From these data, the matching algorithm matched 1,846 pairs, and 1,761 of them are considered correct within a 1 pixel tolerance. This result gives a match yield and reliability of 84.06 and 95.40 %, respectively. These test results together with the results from several other researchers are shown in Table 5. For the known particle location test, the current matching algorithm has a match yield only slightly lower than the ICCRM algorithm (Brevis et al. 2011) and similar reliability percentages among the compared algorithms. The best two results in the known particle location test—the present work and ICCRM algorithm—are both methods utilizing a cross-correlation algorithm to help the tracking results. Compared to other work, the addition of a cross-correlation algorithm improves the tracking performance for the low particle density areas because it provides additional data other than the particle locations and thus increases the reliability of the results at these areas. In the present work, the cross-correlation algorithm is added as an additional term in the proximity matrix, and the weighting is auto-adaptive. In the ICCRM algorithm, the cross-correlation method is the preprocessing stage of the relaxation method, and the weighting is controlled by the correlation threshold level, which is manually selected by the user. For the unknown particle location test, the match yield and reliability of the present work are slightly lower than those of the other algorithms, nevertheless the number of found and matched particles are the highest among all the algorithms.

This unknown particle location result suggests that the particle identification algorithm does not perform very well on these images, yet this can be explained with the following two causes. The first reason is that the particle mask radius has to be set to 1 pixel in order to accurately find the particles in these VSJ#301 images, because the mean particle image diameter is set to 4 pixels. Under this condition, the particle mask radius cannot be reduced anymore, limiting the correlation operation to only perform once. Thus, the CCM algorithm is reduced to a normal PMCM algorithm, which reduces the ability to resolve overlapping particles. The second reason is that the VSJ #301 image does not sum all the intensities for each pixel from each of the overlapping particles, but instead uses only the intensities of the brightest particle. Okamoto et al. (2000) generate VSJ standard PIV images this way because they believe occlusions occur when particle images overlap one another. This may not be practical in some cases, however, since multi-scattering may occur, and a particle image is not only formed by direct illumination but also due to fractions of light scattered from other particles (Raffel et al. 1998). The particle image diameter d_τ can be approximated by the formula (Raffel et al. 1998)

$$d_\tau = c\left(M^2 d_p^2 + d_s^2\right)^{1/2} \tag{14}$$

where M is the magnification of the lens system, d_p is the actual particle diameter, d_s is the diffraction limited spot size defined as follow

$$d_s = 2.44(1 + M^2) f^{\#} \lambda \tag{15}$$

where $f^{\#}$ is the f number defined as the ratio between the focal length and the aperture diameter of the lens, and λ is the wavelength of illuminating light. In general, d_τ is more

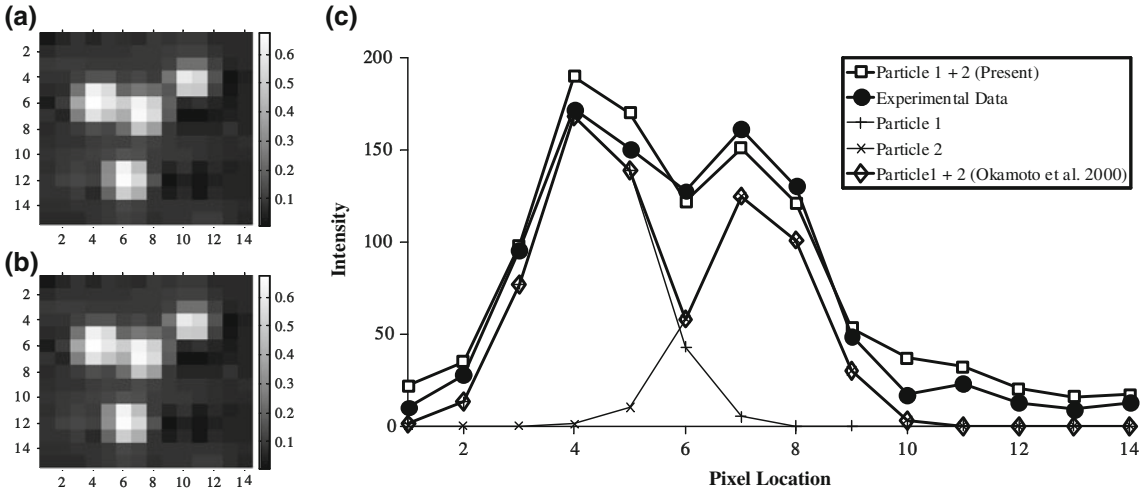

Fig. 11 Comparison of particle image reconstruction performance based on different assumptions. **a** Original image, **b** reconstructed image by current work, **c** comparison of profiles of the 6th *row*

dominated by diffraction effects with smaller particles and more dominated by geometric optics when particles are larger. Thus, in the case of small particles, occlusion may be less of an issue and Okamoto's model may not reconstruct the overlapped particle image very well. To verify this, an experimental image of overlapping particles is examined and reconstructed with the current particle identification method as shown in Fig. 11a, b. The cross-sectional profiles of the 6th row of the actual image and the reconstructed images are shown in Fig. 11c. The overlapping region in the middle of the two particles is underestimated by the occlusion assumption, while the proposed method predicts the profile more accurately. Since the optics assumption used in the present work is different than that used in VSJ standard PIV image generation, the results reflect this difference as higher location error and eventually lower matching performance. In spite of the issues mentioned above, results from the current method are comparable to other methods and show a higher number of found and matched particles, as seen in Table 5.

4.6 Experimental images

The present algorithm was applied to an experimentally obtained shear layer image set. The area viewed was 22 cm by 22 cm, with flow velocities of 10.5 and 22.5 cm/s and a

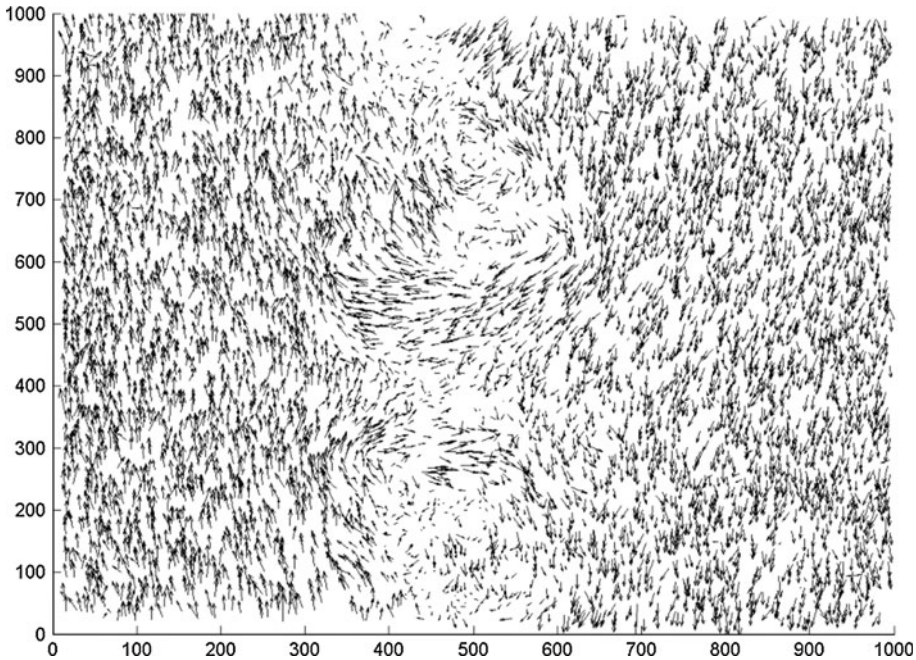

Fig. 12 Shear layer flow field with average of free stream velocity subtracted

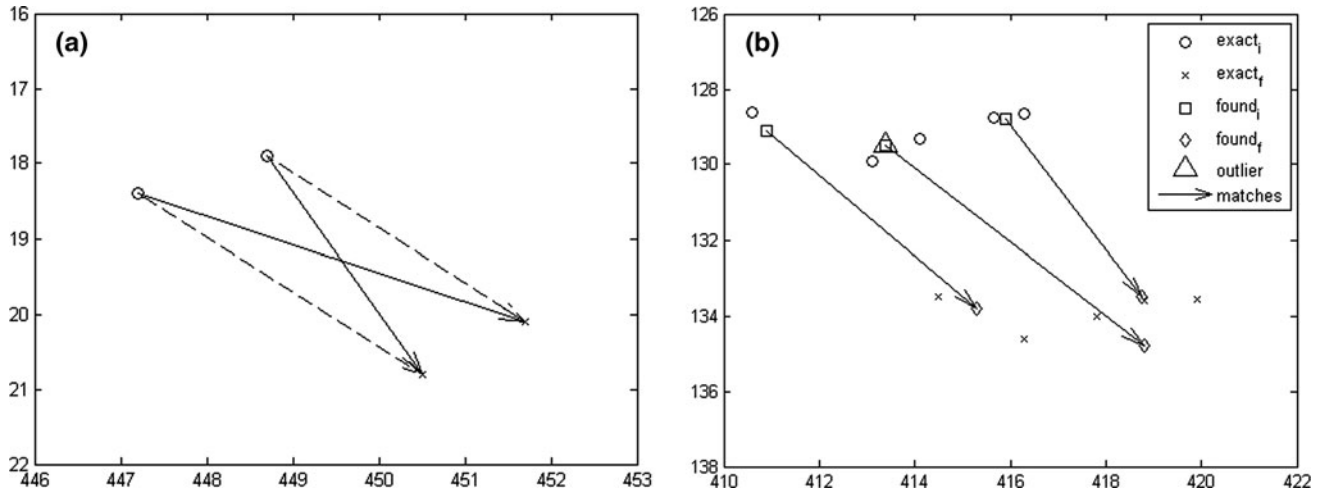

Fig. 13 **a** Example of error due to crossed matches. **b** Errors caused by *peak* finding inaccuracy. *Plot* shows 5 pairs of exact particle *peak locations* and 3 pairs of *peaks* resolved by the particle location identification algorithm (particle diameter of 4 pixels)

Reynolds number, based on a visual shear layer thickness of 1.2×10^4. The apparatus and details of the flow in question are described in Dabiri (2003). The resulting vector field is shown in Fig. 12. The average of the free stream velocities (16.5 cm/s) is subtracted from all the vectors in order to better show the flow structures. The particle identification algorithm found 12,429 and 12,143 particles in frames 1 and 2, respectively. A total of 7,777 matches were found, resulting in a match yield of 64.0 %. This is lower than the results from synthetic images with random particle sizes and intensities (92.6 %; see Table 4). The reason for this lies in the large number of particles passing through the laser sheet in the experimental flow, which appear in only one of the images. To check the effect of these rogue particles on matching results, synthetic images were generated with similar particle image characteristics as the experimental images and particle images were deleted and replaced with randomly located particle images to simulate particles moving into and out of an experimental laser sheet. The results of running the particle identification and matching algorithms on these images demonstrated a linear relationship between the percentage of rogue particle images and the match yield, that is, when 10 % of particle locations were randomized, a roughly 10 % drop in match yield was observed; when 20 % of particle locations were randomized, the match yield dropped by 20 %, and so on.

As an additional check on the current algorithm's ability to process experimental data, images were collected from a uniform flow in a water tunnel with very few observable out of plane losses. The flow velocity was 50.0 cm/s, the area viewed was 29 by 29 mm with a magnification of 0.22, and flow was seeded with 44 micron particles. The match yield was 85.2 %, which is similar to the synthetic images with random particle intensity and diameter (92.6 %). These results suggest that the low match yield for the shear layer images is indeed due to out of plane losses and that the current algorithm is capable of processing real images.

4.7 Sources of error

Two main sources of error tend to affect the known and unknown particle location tests. The first is the result of particle pairs or triads which cross one another. Even with slightly larger separation, the matching algorithm has difficulty in correctly choosing which particles in the first and second images are matches. These crossed vectors can account for as many as half of erroneous matches (those with an error >1 pixel). An outlier detection algorithm is applied to matching results, but is also unlikely to detect these crossed vectors as they do not often deviate seriously from the surrounding flow field. An example is shown in Fig. 13a. A simple routine is used to detect these crossed vectors and either remove or correct them. This resulted in reducing the RMS errors, on average, by 16 %

In addition to crossed matches, when the particle location identification method is used, the primary source of unreliable matches lies in the ability to accurately locate the peaks of overlapping particles. In high density images in particular, a particle blob can easily contain four or more particles. Small changes in relative locations among these particles from one image to the next can alter the results of particle location identification from one frame to the next and sometimes results in a poor representation of flow behavior. An example is shown in Fig. 13b.

5 Conclusion

In conclusion, a novel technique for PTV is proposed and tested focus on dealing with larger and severely overlapped particle image field. An improved particle identification algorithm using both CCM and 2-D surface Gaussian fitting is developed to improve the yield of identifying overlapping particles. Particle matching based on vision principles is used with guiding PIV technique to provide accurate and robust particle tracking. Synthetic image tests showed that particle overlap can be resolved up to a 60 % overlap at noise levels of 5 % or less, and the velocity profile of a moving wall flow reconstructed is in good agreement with the analytic solution. Sensitivity tests were performed to describe optimum conditions for the use of this PTV algorithm. The best results were obtained with particle densities with particle overlap up to 50 %, small particle image diameters, and pixel per pixel gradients up to 0.3. The algorithm was also tested with standard VSJ PIV images, and the results were compared with other published works. The current method compared favorably with existing PTV methods with known particle locations. The slightly lower reliability of matches obtained using the particle location algorithm was attributed to the construction of the artificial VSJ images. Experimental images of a shear layer with a particle image density 0.02 were tested, and a match yield of 63.8 % was obtained.

Acknowledgments The authors gratefully acknowledge the support of the National Institutes of Health (R01 RR023190-04), the Murdock Trust Foundation, and the insightful comments provided by the reviewers who have added to the value of this paper.

References

Adrian RJ, Yao CS (1985) Pulsed laser technique application to liquid and gaseous flows and the scattering power of seed materials. Appl Opt 24:44–52

Agui JC, Jimenez J (1987) On the performance of particle tracking. J Fluid Mech 185:447–468

Angarita-Jaimes NC, Roca MG, Towers CE, Read ND, Towers DP (2009) Algorithms for the automated analysis of cellular dynamics within living fungal colonies. Cytom A 75(9):768–780

Baek SJ, Lee SJ (1996) A new two-frame particle tracking algorithm using match probability. Exp Fluids 22(1):23–32

Brady MR, Raben G, Vlachos PP (2009) Methods for Digital Particle Image Sizing (DPIS): Comparisons and improvements. Flow Meas Instrum 20(6):207–219

Brevis W, Nino Y, Jirka GH (2011) Integrating cross-correlation and relaxation algorithms for particle tracking velocimetry. Exp Fluids 50(1):135–147

Cowen EA, Monismith SG (1997) A hybrid digital particle tracking velocimetry technique. Exp Fluids 22(3):199–211

Dabiri D (2003) On the interaction of a vertical shear layer with a free surface. J Fluid Mech 480:217–232

Duncan J, Dabiri D, Hove J, Gharib M (2010) Universal outlier detection for particle image velocimetry (PIV) and particle tracking velocimetry (PTV) data. Meas Sci Technol 21(5): 057002

Elghobashi S (1994) On predicting particle-laden turbulent flows. Appl Sci Res 52(4):309–329

Gharib M, Kremers D, Koochesfahani MM, Kemp M (2002) Leonardo's vision of flow visualization. Exp Fluids 33(1):219–223

Gunes H, Sirisup S, Karniadakis GE (2006) Gappy data: to Krig or not to Krig? J Comput Phys 212:358–382

Keane RD, Adrian RJ, Zhang Y (1995) Super-resolution particle imaging velocimetry. Meas Sci Technol 6(6):754–768

Kim HB, Lee SJ (2002) Performance improvement of two-frame particle tracking velocimetry using a hybrid adaptive scheme. Meas Sci Technol 13(4):573–582

Liao Q, Cowen EA (2005) An efficient anti-aliasing spectral continuous window shifting technique for PIV. Exp Fluids 38(2): 197–208

Luo B, Hancock ER (2002) Iterative procrustes alignment with the EM algorithm. Image Vis Comput 20:367–369

Marxen M, Sullivan PE, Loewen MR, Jahne B (2000) Comparison of Gaussian particle center estimators and the achievable measurement density for particle tracking velocimetry. Exp Fluids 29(2): 145–153

Mikheev AV, Zubtsov VM (2008) Enhanced particle-tracking velocimetry (EPTV) with a combined two-component pair-matching algorithm. Meas Sci Technol 19(8):085401

Nogueira J, Lecuona A, Rodriguez PA (2005) Limits on the resolution of correlation PIV iterative methods. Fundamentals. Exp Fluids 39(2):305–313

Nogueira J, Lecuona A, Rodriguez PA (2001a) Identification of a new source of peak locking, analysis and its removal in conventional and super-resolution PIV techniques. Exp Fluids 30(3):309–316

Nogueira J, Lecuona A, Rodríguez PA (2001b) Local field correction PIV, implemented by means of simple algorithms, and multigrid versions. Meas Sci Technol 12(11):1911–1921

Ohmi K, Li HY (2000) Particle-tracking velocimetry with new algorithms. Meas Sci Technol 11(6):603–616

Okamoto K, Nishio S, Saga T, Kobayashi T (2000) Standard images for particle–image velocimetry. Meas Sci Technol 11(6):685–691

Otsu N (1979) A threshold selection method from gray-level histograms. IEEE Trans Syst Man Cybern 9:62–66

Panday SP, Ohmi K, Nose K (2011) An ant colony optimization based stereoscopic particle pairing algorithm for three-dimensional particle tracking velocimetry. Flow Meas Instrum 22(1):86–95

Pilu M (1997) A direct method for stereo correspondence based on singular value decomposition. In: IEEE computer vision and pattern recognition conference, San Juan, Puerto Rico, pp 261–266

Ponchaut N (2005) Part I: 3DPTV—advances and error analysis; part II: extension of Guderley's solution for converging shock waves. PhD thesis, California Institute of Technology

Ponchaut N, Mouton C (2005). 3-D particle tracking velocimetry method: advance and error analysis. GALCIT report FM2005. 004

Raffel M, Willert C, Kompenhans J (1998) Particle image velocimetry: a practical guide. Springer, Berlin

Ruhnau P, Guetter C, Putze T, Schnorr C (2005) A variational approach for particle tracking velocimetry. Meas Sci Technol 16(7):1449–1458

Saga T, Kobayashi T, Segawa S (2003) Development and evaluation of an improved correlation based PTV method. In: 6th international symposium on fluid control, measurement and visualization, Sherbrooke, Canada

Scarano F (2003) Theory of non-isotropic spatial resolution in PIV. Exp Fluids 35(3):268–277

Schonemann PH (1966) A generalized solution of the orthogonal procrustes problem. Psychometrika 31:1–10

Scott G, Longuet-Higgins H (1991) An algorithm for associating the features of two images. Biol Sci 244:21–26

Shindler L, Moroni M, Cenedese A (2011) Spatial–temporal improvements of a two-frame particle-tracking algorithm. Meas Sci Technol 21(11):115401

Song X, Yamamoto F, Iguchi M (1999) A new tracking algorithm and removal of spurious vectors using Delaunay tesselation. Exp Fluids 26(4):371–380

Stellmacher M, Obermayer K (2000) A new particle tracking algorithm based on deterministic annealing and alternative distance measures. Exp Fluids 28(6):506–518

Takehara K, Adrian RJ, Etoh GT (2000) A Kalman tracker for super-resolution PIV. Exp Fluids 29(7):s034–s041

Takehara K, Etoh T (1999) A study on particle identification in PTV-particle mask correlation method. J Vis 1(3):313–323

Uemura T, Yamamoto F, Ohmi K (1989) A high speed algorithm of image analysis for real time measurement of two-dimensional velocity distribution. ASME FED 85:129–134

Ullman S (1979) The interpretation of visual motion. MIT Press, Cambridge